

Persistence diagrams for exploring the shape variability of abdominal aortic aneurysms

Dario Arnaldo Domanin*, Matteo Pegoraro†, Santi Trimarchi‡§,
Maurizio Domanin‡§, Piercesare Secchi¶

February 14, 2024

Abstract

Abdominal Aortic Aneurysm consists of a permanent dilation in the abdominal portion of the aorta and, along with its associated pathologies like calcifications and intraluminal thrombi, is one of the most important pathologies of the circulatory system. The shape of the aorta is among the primary drivers for these health issues, with particular reference to all the characteristics which affects the hemodynamics. Starting from the computed tomography angiography of a patient, we propose to summarize such information using tools derived from Topological Data Analysis, obtaining persistence diagrams which describe the irregularities of the lumen of the aorta. We showcase the effectiveness of such shape-related descriptors with a series of supervised and unsupervised case studies.

Keywords: topological data analysis; abdominal aortic aneurysm; persistent homology.

1. Introduction

One of the main drivers of contemporary medical research is the idea of *personalized medicine*, which aims at providing better targeted treatments to improve therapy outcomes. The achievement of such a challenging task relies primarily on two factors: the constantly increasing amount of data made available by modern data collecting pipelines, like medical imaging, and the joint efforts of clinicians and statisticians, trying to unpack the valuable information contained in the provided data.

The statistical understanding of any phenomenon is always limited by the interpretable methods and algorithms that the analyst can resort to. As a consequence, there is an increasing need of new and original statistical methods aimed at the analysis of different and heterogeneous kinds of complex data, validated and interpreted by the expert clinician. In many medical situations, especially those related to imaging data, many complexities arise because of the difficulty in decoupling interesting variability between statistical units from that which the clinician considers as ancillary. This problem is at the root of *object oriented data analysis* Marron and Dryden (2021), whose foundational principles focus on data representation, by embedding the atoms of the statistical analysis in a suitable mathematical space where their variability of interest can be captured and explored.

In this work we consider the problem of analysing and characterising *abdominal aortic aneurysms* (AAAs) eliciting the information contained in the shape of blood vessels with tools from algebraic topology.

*. Moxoff, Milano

†. Department of Mathematical Sciences, Aalborg University

‡. Department of Clinical Sciences and Community Health, Università degli Studi di Milano

§. Dipartimento Area Cardio-Toraco Vascolare, S.C. Chirurgia Vascolare, Fondazione IRCCS Cà Granda Ospedale Maggiore Policlinico

¶. MOX – Department of Mathematics, Politecnico di Milano

Abdominal Aortic Aneurysm consists of a permanent dilation of at least 1.5 times the expected diameter of the abdominal portion of the aorta (see Figure 1a), the biggest artery of the human body Sonesson et al. (1994), characterized by chronic inflammation processes in the inner layers with degradation or redistribution of elastin and collagen Wilson et al. (2001) under the haemodynamical stress Dua and Dalman (2010). Such dilatation can evolve asymptotically towards the progressive enlargement of the vessel up to its rupture which is frequently fatal, making it one of the most prominent pathologies of the circulatory system.

Most of the literature dealing with the analysis of AAAs focuses on the growth rate of small AAAs Parr et al. (2011); Kauffmann et al. (2012), in order to prevent their rupture and identify the necessity of surgery, leveraging on shape-related or biomechanical numerical features. See, for instance, Lee et al. (2018); Hirata et al. (2020); Kontopodis et al. (2023); Zhu et al. (2020); Lindquist Liljeqvist et al. (2021). Differences between these works appear in the statistical methodology employed for prediction, but, mostly, in the kind of features collected: AAA and intraluminal thrombus' diameter, volume, axes are considered in most studies; Kontopodis et al. (2023), Lindquist Liljeqvist et al. (2021) and others include also biomechanical indices - like peak wall stress and peak wall rupture indices - and clinical variables, showing improved predictions.

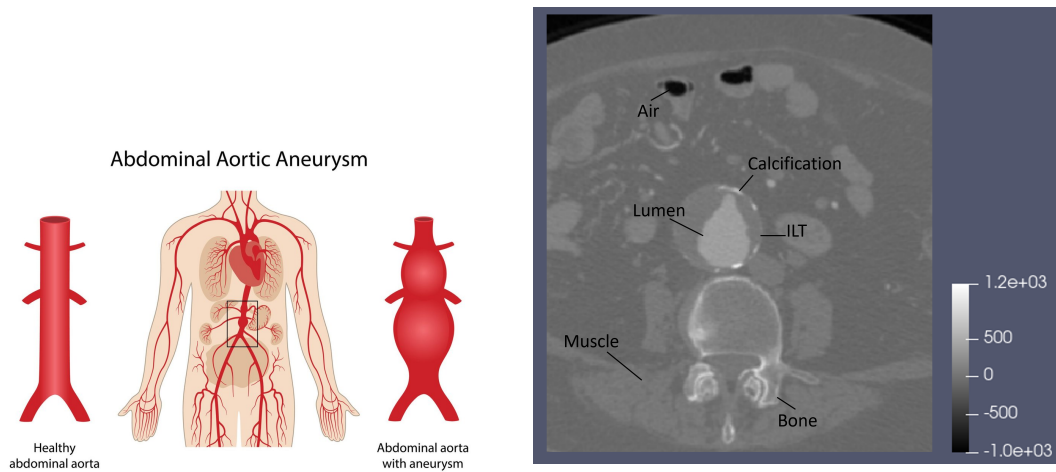
The aim of our work is different and is more in line with Kyriakou et al. (2019b); indeed, we want to establish a new mathematical representation of the geometric complexity of the aorta and of the surrounding blood vessels. A deep dive on the heuristic power of this new representation is the main aim of this paper; we leave to future work the assessment of its predictive power in terms of growth rate of small AAAs. Nevertheless, most of the information conveyed by morphological and shape related variables is also contained in our novel representation, which, however, has the extra advantage of summarizing additional information which is harder to convey in terms of numerical variables; like, for instance, a quantification of the calcifications along the blood vessels.

To obtain such representation we resort to algebraic topology Munkres (2018) and, in particular, to *persistent homology* Edelsbrunner and Harer (2022), one of the most diffused frameworks in Topological Data Analysis (TDA). By introducing a carefully studied and application-driven filtering function, we are able to synthesize the Computed Tomography Angiographies (CTAs) of patients - a particular kind of medical images, see Figure 1b - capturing the statistically sufficient features of their *shapes*. Moving from a preliminary segmentation pipeline, already well established and whose goal is to turn CTA images into 3D meshes, we transform them into mathematical objects called *persistence diagrams*. Thus, the statistical analysis is moved from the initial CTA images to their representations embedded in the space of persistence diagrams. To demonstrate the effectiveness of this representation we propose a number of analyses characterized by the simplicity of the pipeline, but heavily relying on the power of the chosen representation.

The approach pursued in this work paves the way for more refined analyses - for instance on the growth rate of small AAAs - grounded on the same topological representation and aimed at providing clinicians with valuable insights and checkpoints to complement their current analyses. We also foresee applications of analogous filtering functions to other contexts needing similar shape-dependent characterizations, such as cerebral aneurysm and the development of the atheromatous plaque in arterial vessels.

1.1 Outline

In Section 2 we give a brief overview of Abdominal Aortic Aneurysms and their related pathologies. Then, in Section 3, we concisely describe the segmentation pipeline to obtain the meshes from the CTA scans. Section 4 is devoted to presenting the (normalized) radial filtration function and the associated persistence diagrams. Section 5 is entirely focused on reading patient-related information from persistence diagrams. In Section 6 we propose a number of data analysis situations which are easily tackled with the use of persistence diagrams. All the packages and softwares we employ for visualization and analyses are



(a) Schematic view of the circulatory system with shades of grey differentiate between different highlighted the abdominal portion of the aorta, organs and tissues. This allows both the clinician with both an healthy and aneurysmatic example. Image from <https://www.vascularcures.org/> and the algorithm to execute the segmentation process.

(b) Coronal slice of a CTA scan. Different shades of grey differentiate between different highlighted the abdominal portion of the aorta, organs and tissues. This allows both the clinician with both an healthy and aneurysmatic example. Image from <https://www.vascularcures.org/> and the algorithm to execute the segmentation process.

Figure 1: Schematic representation of an Abdominal Aortic Aneurysm and a CTA scan.

reported in Section 7. Finally, Section 8 ends the manuscript with a discussion and a conclusion. The Appendix contains some further technical details.

2. Abdominal Aortic Aneurysm

Abdominal Aortic Aneurysm is the most common aortic pathology. The incidence of Ruptured Abdominal Aortic Aneurysm (RAAA) is up to 17.5 per 100,000 person/year in Western countries Mealy and Salman (1988). It is mainly located between the renal and the iliac arteries, which can also present dilatations on their owns called *iliac aneurysms*. The healthy segment of the abdominal aorta above the dilatation is defined as *aortic neck*.

Two main features characterize the aneurysm: *intraluminal thrombus* (ILT), thrombus for short, and wall *calcification*. The former is the stratification of several blood particles in the inner layers, the latter is the accumulation of calcium in the aortic wall responsible of its stiffening. Both negatively affect the aorta changing its physiological behavior by modifying the *lumen's* structure, the region where the blood flows, with bumps and irregularities.

Since vessel's morphology plays a major role in local haemodynamics which, in turn, determines the development of the AAA Piccinelli et al. (2013), Vergara et al. (2017), in this study we focus on the aortic lumen. Hence we are only interested in the information directly associated to the shape of the lumen. For this reason, calcium formations which could occur on the external part of a thrombus will be disregarded.

3. Data

In this section we outline our complex pipeline for data gathering and pre-processing.

3.1 CTA scans

The most used and effective method for anatomy visualization is Computed Tomography Angiography. CTA is used to get a visualization of the human body and is realized with emission of X-rays through a tomograph. A CTA scan consists of a 3-dimensional image

of a region of interest in the form of a volume composed by voxels with different shades of grey. Each shade is associated to a different tissue, making it possible to distinguish not only between fat, bones and muscle but also artery, intraluminal thrombus (ILT) and calcification - see also Figure 1b.

The data considered in this work consist of 48 CTA scans of the abdominal region, 24 of which picture a pathological aorta. To secure data consistency, the following criteria have been applied:

- AAA greater than 3.5cm in diameter;
- infrarenal AAA, not extended above the renal arteries, and presence of the aortic neck;
- CTA with high resolution and contrast, to assure high quality data;
- non-minor and non-pregnant patients.

All the CTA scans are provided by Ospedale Maggiore Policlinico. Patients with healthy aortas have been collected from the Policlinico's archive while the patients affected by AAA come from the Vascular Surgery Unit. For privacy reasons, all data are anonymized.

3.2 Segmentation Pipeline

The primary function of a CTA scan in this study is to enable the segmentation of the aortic lumen, rather than for visualization purposes. Aortic segmentation refers to the process of obtaining a three-dimensional reconstruction of the lumen via a finite number of points, as visually described in Figure 2. The product of the segmentation is a mesh, consisting of a set of vertices, edges and cells that form a net of triangles. Segmentation is made possible thanks to a pipeline provided by *Moxoff*¹.

The tract of the vessel considered in this study ranges between the distal renal artery and the common iliac arteries, including the area eventually affected by the AAA and iliac aneurysms, using manually selected points - see also Figure 1b. The pipeline used to perform the segmentation relies mainly on an edge-based technique with the support of thresholding and region-based methods to improve performances and results. Following Fosbinder and Orth (2011), thresholding makes an initial guess of the points belonging to the lumen. Then region-based and edge-based techniques Sonka and Fitzpatrick (2009) help with recognition of the rounded shape of the vessel, when projected on the coronal plane. In this way, a label is applied to each of the voxels of the CTA scan creating a volume whose surface is extracted and triangulated.

The resolution of the segmentation (i.e. the average length of the edges) is 1.0mm , empirically chosen to balance the trade off between accuracy and computational costs.

A by-product of the segmentation is the *centreline*. Roughly speaking, the centerline is a continuous curve in space that represents the center of the vessel lumen and makes for a powerful descriptor of its shape. Among the several methods proposed in the literature for its identification, we use the algorithm provided by Antiga et al. (2008) within VMTK, the Vascular Modeling Toolkit², which generates a mathematical object stable to perturbations of the vessel's lumen surface. Identification of the centerline is of greatest importance for singling out points on the lumen surface considered as peripheral.

4. Object Representation through Persistent Homology

We now describe the mathematical objects used to represent the atoms of our statistical analysis, that is to represent the meshes obtained from segmentation of the CTAs of the patients. The key element that drives the upcoming construction is a function defined on a mesh, called *filtering* function, with the property that the morphological features we are interested in appear as local minima and local maxima of this function. In particular,

1. <https://www.moxoff.com/en/>
2. <http://www.vmtk.org>

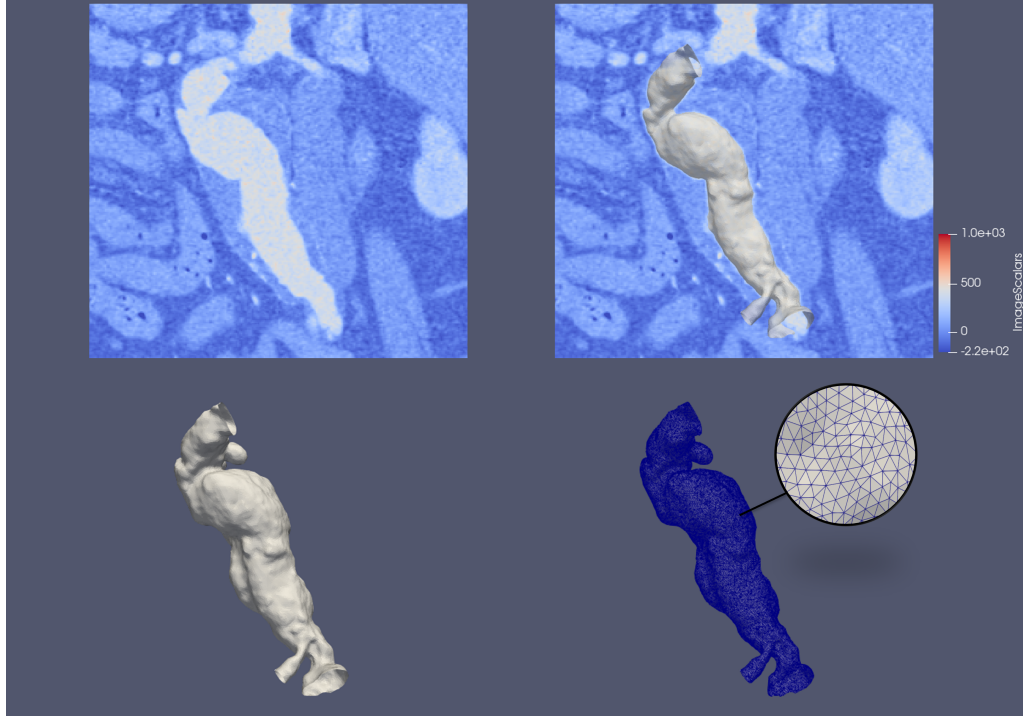


Figure 2: A schematic view of the segmentation process, starting from the CTA scan and obtaining the final mesh representing the portion of interest of the Aorta and the ilia.

the filtering function should capture inward and outward bumps of a blood vessel, so it must be based on some sort of radial distance.

4.1 Filtrations and Homology

Consider a triangular mesh $K \subset \mathbb{R}^3$ as the union of the set of its triangles, K^2 , the set of its edges, K^1 , and the set of its vertices K^0 . This data amounts to a *simplicial complex* Munkres (2018) which is the combinatorial starting point of persistent homology. Every element in K is called a simplex: *0-simplex* if it is a vertex, *1-simplex* if it is an edge and *2-simplex*, if it is a triangle.

To define the *radial filtering function* f , we start with a function $f : K^0 \rightarrow \mathbb{R}$ defined on the vertices of the mesh, and we suitably extend it to the whole K . Let $\gamma \subset \mathbb{R}^3$ be the centerline of the blood vessel. For every vertex $v \in K^0$ define:

$$f(v) = \min_{p \in \gamma} \|v - p\|,$$

that is, the distance of the vertex v from the centreline. For every $\sigma \in K^1 \cup K^2$, being it an edge or a triangle, we extend f as follows:

$$f(\sigma) = \max_{v \in \sigma \cap K^0} f(v).$$

This extension is motivated by the following facts: it is easy to handle computationally and, by standard topology results Edelsbrunner and Harer (2022), it is equivalent to the piecewise linear extension on the mesh of the f defined on its vertices.

We now use $f : K \rightarrow \mathbb{R}$ to order the vertices, edges and triangles of K into a filtration of simplicial complexes. For $t \in \mathbb{R}$, consider the simplicial complex K_t defined by the sublevel set

$$K_t = f^{-1}((-\infty, t]).$$

Since f can assume only a finite number of distinct values, let them be $t_0 < t_1 < \dots < t_m$ to obtain the filtration $\{K_{t_i}\}$ of simplicial complexes, such that

$$K_{t_0} \subset K_{t_1} \subset \dots \subset K_{t_m} = K.$$

Some pivotal observations are in order; they can be visualized by looking at Figure 3.

First we define the path connected components of f . An inward bump of the vessel corresponds to a local minimum of f ; when it appears in the filtration $\{K_{t_i}\}$, a new path connected component is “born” in the sublevel sets of f ; see Figure 3a. That path connected component persists until it is merged with other path connected components, born at lower local minima. Visually, for this to happen, one needs that the whole inward bump generated by the local minimum is added to the filtration, so that different path connected components can meet at local maxima or saddle points. An outwards bump, instead, produces a loop which surrounds its boundary - see Figure 3b. As the filtration value increases and the simplicial complexes grow, this loop, which encloses the local maximum of the outward bump, becomes smaller and smaller, eventually superimposing to the local maximum itself, and “dying” - see Figure 3b. There is also another way in which loops are created, as showcased by Figure 3c: the tubular structure of the blood vessels allows also loops that go around the centerline. Two such loops are equivalent if they can “slide” on the mesh, superimposing one with the other - like the top and the bottom black loops in Figure 3c.

Thus, the mesh is transformed through f into the filtration of simplicial complexes $\{K_{t_i}\}$; identifying along the filtration “births” and “deaths” of path connected components and loops, characterizes the blood vessel in terms of the irregularities of its lumen.

Topologically speaking path connected components and loops are captured, respectively, by homology in dimension 0 and 1, which we now formally and briefly define. For more details see Edelsbrunner and Harer (2022).

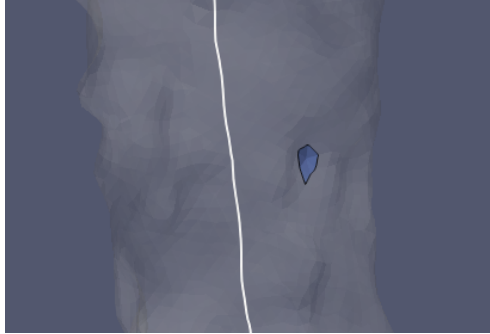
For notational coherence with the literature, we refer to (oriented) triangles and edges in a simplicial complex via the set of their vertices enclosed by squared brackets: e.g. $[x_0, x_1, x_2]$ for a triangle, i.e. a 2-simplex, and $[x_0, x_1]$ for an edge, i.e. 1-simplex. Given a simplicial complex K_{t_i} , for $n = 0, 1, 2$ we generate the vector space $C_n(K_{t_i})$ over the field $\mathbb{Z}_2 = \{0, 1\}$, by considering the set of all finite formal sums of the n -simplices belonging to K_{t_i} . For $n = 1, 2$, the boundary operators $\partial_n : C_n(K_{t_i}) \rightarrow C_{n-1}(K_{t_i})$ are then defined by setting

$$\partial_n(\sigma) = \sum_{i=0}^n \sigma_{-i},$$

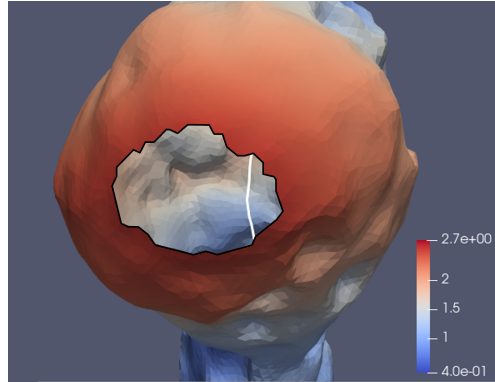
when σ is an n -simplex, and by extending linearly to the whole vector space $C_n(K_{t_i})$; here σ_{-i} is the (oriented) $(n - 1)$ -simplex obtained from σ by deleting its i -th vertex - e.g. $[x_0, x_1, x_2]_{-1} = [x_0, x_2]$. The boundary operator ∂_0 maps $C_1(K_{t_i})$ in the trivial vector space whose only element is 0. We can now introduce the spaces of n -boundaries and n -cycles of K_{t_i} : $Z_n(K_{t_i}) = \ker(\partial_n)$ are the n -cycles and $B_n(K_{t_i}) = \text{Im}(\partial_{n+1})$ are the n -boundaries of K_{t_i} . Finally, we define the n -dimensional simplicial homology groups $H_n(K_{t_i}) = Z_n(K_{t_i})/B_n(K_{t_i})$. Note that the quotient $Z_n(K_{t_i})/B_n(K_{t_i})$ is well defined since $\partial_n \circ \partial_{n+1} = 0$. In particular, linearly independent vectors in $H_1(K_{t_i})$ are independent loops which are not filled by triangles (see Figure 3, right), and linearly independent vectors in $H_0(K_{t_i})$ are points which are on different path connected components (see Figure 3, left). Elements in $H_n(K_{t_i})$ are referred to as homology classes or (equivalence) classes of n -cycles. Tracking down the evolution of $H_1(K_{t_i})$ and $H_0(K_{t_i})$ along the filtration $\{K_{t_i}\}$ returns the information on the vessel shape we are going to explore in this paper.

4.2 Normalization

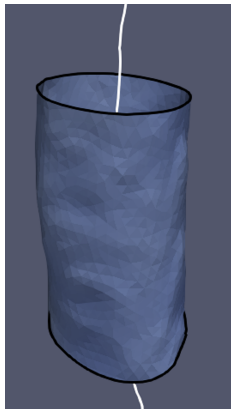
One further step is needed to ensure a fair comparison between filtrations obtained from vessels of different patients.



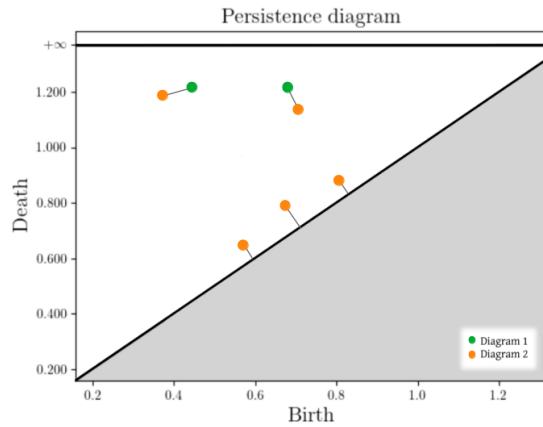
(a) A path connected component created by an inward bump, in the sublevel set filtration defined in Section 4.1. Path connected components created by other inward bumps merge with each other at saddle points or local maxima.



(b) A loop created by an outward bump, in the sublevel set filtration defined in Section 4.1. When the whole bulge is contained in the filtration, the loop disappears.



(c) Loops generated by the tubular structure of the mesh.



(d) Two persistence diagrams and the optimal matching between them giving the bottleneck distance.

Figure 3: Path connected components, loops and persistence diagrams.

As it is often the case with shape analysis, the magnitude or the size difference between patients can act as a confounding factor to the point of overshadowing the shape variability, which is the one we are interested in. For instance, different patients can have different healthy dimensions for the aorta and for the iliacs, making it harder to compare them by contrasting the filtrations and the homology groups generated by their respective filtering functions. To avoid this potential bias in the analysis, we resort to a normalization process, expressing all distance values relative to the healthy size of the patient’s aorta, i.e. the average neck radius. We recall that the aortic neck is in fact the first healthy tract of the aorta, right below the distal renal artery. Its diameter is equal to an healthy aortic diameter, it does not have high variability and it summarizes the size factor of the aorta, in accordance with the scientific literature Kyriakou et al. (2019a). So, for each patient, the filtering function values have been divided by its average neck radius, obtained as reported in Appendix A.

On top of that, since different portions of the blood vessel are characterized by a different relative radius, with respect to the neck’s radius, we can in fact relate the normalized filtering function values to morphological features of the aorta, see Section 5.

4.3 Persistence Diagrams

Looking at the homology groups obtained from a filtration is not practical for applications, but there is a very interpretable and concise summary of the information contained in the sequence of $H_n(K_{t_i})$, called the *persistence diagram* in dimension n . These are the objects that we are going to use to represent data.

A persistence diagram is a finite collection of points in \mathbb{R}^2 - also called *persistence pairs* -, with every point $p = (b, d)$ representing the birth and the death of a persistent homology class. In particular, the birth of an homology class is the first “time t ” it appears along the filtration, while the death time happens when the class merges with another class born earlier. For example: a local minimum of the filtering function, indicative of a bump in the vessel, induces a path connected component which is born at the value of the minimum, Figure 3a; such path connected component carries on, or *persists*, along the filtration, and dies when it merges with a path connected component born earlier, therefore associated to a lower local minimum. The absolute difference between the times of birth and death is clearly related to the prominence of the bump, and is called *persistence* of the homological feature. Note that points can appear multiple times in the same persistence diagram.

4.4 Populations of Persistence Diagrams

Lastly, it is possible to compare and analyze the topological information carried by different persistent diagrams by defining suitable metrics, satisfying formal stability results; for an extensive review see, for instance, Edelsbrunner and Harer (2022). It is thus possible to quantify the dissimilarity of two different diagrams and perform classification, clustering and dimensionality reduction on populations of diagrams.

To simplify the upcoming formulas, let

$$D = \{(b_1, d_1), \dots, (b_n, d_n) \mid n \in \mathbb{N}, b_i, d_i \in \mathbb{R} \cup \{\infty\}, b_i < d_i\} \cup \{(b, d) \mid b, d \in \mathbb{R}, b = d\}.$$

represent a persistence diagram. Given two diagrams D_1 and D_2 and $p \geq 1$, the p -Wasserstein distance between them is:

$$W_p(D_1, D_2) = \left(\inf_{\gamma} \sum_{x \in D_1} \|x - \gamma(x)\|_{\infty}^p \right)^{1/p} \quad (1)$$

where the inf is taken over all bijections γ between diagrams D_1 and D_2 . In other words we measure the distances between the points of the two diagrams, pairing each point of a diagram either with a point on the other diagram, or with a point on $y = x$ (see Figure 3d). Each point can be matched once and only once. The minimal cost of such

matching provides the distance. The case $p = \infty$ is usually referred to as the bottleneck distance and has the following form:

$$W_\infty(D_1, D_2) = \inf_{\gamma} \sup_{x \in D_1} \|x - \gamma(x)\|_\infty .$$

Note that, to compare two persistence diagrams, we do not need to establish a relationship between the generating meshes. In particular this means that no alignment or registration is needed to proceed with the analysis; this is the ancillary source of variability between patients we are not interested in.

Finally, let us mention an important stability result Cohen-Steiner et al. (2005). Given two filtering functions $f, g : K \rightarrow \mathbb{R}$ and their respective persistence diagrams $D(f), D(g)$:

$$W_\infty(D(f), D(g)) \leq \|f - g\|_\infty ,$$

meaning that persistence diagrams are a faithful representation of the functions, in terms of the sup-norm.

Closing this section on persistent homology, we point out the existence of representations alternative to persistence diagrams, for instance persistence landscapes Bubenik (2015), persistence images Adams et al. (2017), persistence silhouettes Chazal et al. (2015), accumulated persistence functions Biscio and Møller (2019). All of these come with their own properties and stability results and can be used for analyses which are possibly more refined or more tailored to the application of interest.

5. Reading a persistence diagram

To understand the descriptive power of the persistence diagrams obtained with the pipeline illustrated in the previous section, a parallel reading of the original mesh and the associated diagrams has been made for every patient in the study, connecting the most important aortic wall features - such as AAA, calcifications and thrombus - to the diagram points.

All the results contained in the upcoming subsections have been manually verified by simultaneously looking at the persistence diagram, the simplicial complexes and the CTA scans, with the support of the collaborating clinicians.

5.1 The Effect of Normalization

We have anticipated in Section 4.2 that normalization is instrumental for comparing different patients since it allows for the appraisal of the distance from the centerline when a persistence pair is created or ceases to exist, relatively to the size of the mean aortic neck radius. Normalization is, in fact, also significant for the identification of the portion of the aorta where the change in homology occurs, locating it on a specific section of the vessel. Note that the diameter of the vessel differs along the aorta, especially after the aortic bifurcation. In fact, the diameter of a healthy abdominal aorta is typically $17.5 \pm 2.1mm$, larger than that of an healthy iliac artery, $10.85 \pm 1.69mm$; see Pedersen et al. (1993); Kim et al. (2022). Although significant differences in the dimension of the aorta for males and females occur, the proportion between the diameter of the main aorta and that of the iliac branches are similar. Thus:

- when an homology class is born (or dies) at a value close to the mean neck's radius, i.e. a value close to 1, the change must be located at the same distance from the centerline as the aortic mean neck's radius, hence on the healthy portion of the aorta. The only exception being an iliac aneurysm, whose presence will be discussed later in Section 5.2;
- in the cohort of the patients considered in this study, the diameter of healthy iliacs is around 40-70 % of the respective aortic mean neck's radius. Thus, changes in homology located on the iliac arteries occur when the normalized distance assumes values in the range of [0.4–0.7];
- lastly, patients affected by AAA can instead have a more variable range, up to 7 and more in the most concerning cases.

Figure 4 depicts a schematic visualization of these facts.

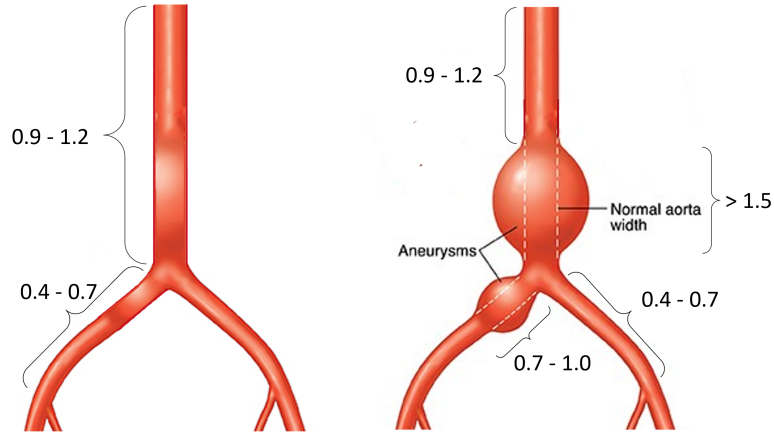


Figure 4: A schematic view of the aorta, with the normalized distances from the centerline made explicit. Image modified from <https://prescrivere.blogspot.com/>.

5.2 Notable Pairs

By combining the information given by birth, death, persistence and type of pairs of points in the persistence diagram, it is possible to identify *notable pairs*, that is persistence pairs shared among patients with similar characteristics associated with a specific aortic region.

5.2.1 STRUCTURAL PAIRS

The first class of points we consider are those associated to an infinite persistence, i.e. such that $d = \infty$. These points correspond to features which are born at a certain filtration value, but which never die, and so persist up to ∞ . They indicate structural features shared by all aortas. In particular, each filtration coming from a correctly segmented aorta must have exactly three points with infinite persistence: one associated to 0-cycles and two associated two 1-cycles.

Indeed, the mesh representing the aorta should be *homotopy equivalent* Edelsbrunner and Harer (2022) to a finite cylinder with a hole, which, in turn, is equivalent to an eight figure: two circles glued in one point, see Figure 5. Roughly speaking, two objects are homotopy equivalent if, starting from one, it is possible to obtain the other using stretching and bending but not tearing. Homotopy equivalence preserves homology and so each mesh should feature a connected component with two independent 1 dimensional loops as can be seen in Figure 5.

These three points, representing the most persistent homological features, can also be used as indication of the correct representation provided by the mesh itself, proving the deep connection between the persistence diagram and the aorta. In fact, if a persistence diagram shows additional points with infinite persistence, this signals an error during the segmentation phase, such as the creation of non-connected points or the presence of artificial holes in the mesh.

5.2.2 ILIAC ANEURYSM

Now we tackle the problem of identifying iliac aneurysms; the reader should refer to Figure 6 and Figure 7 to get a visual description of the content of this section.

Aneurysms can affect one or both the iliac arteries, in the same way as they affect the abdominal aorta, resulting in a stretch of the wall - see Figure 7c. An iliac aneurysm can also be associated with calcification (as in Figure 7) and thrombus, just as the AAA.

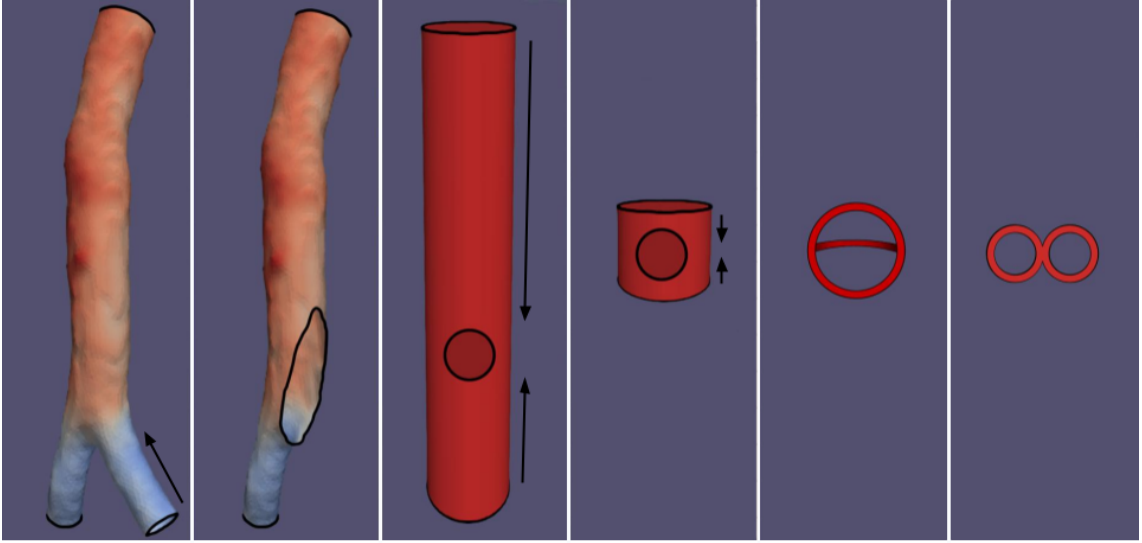


Figure 5: All the objects in this figure are homotopy equivalent.

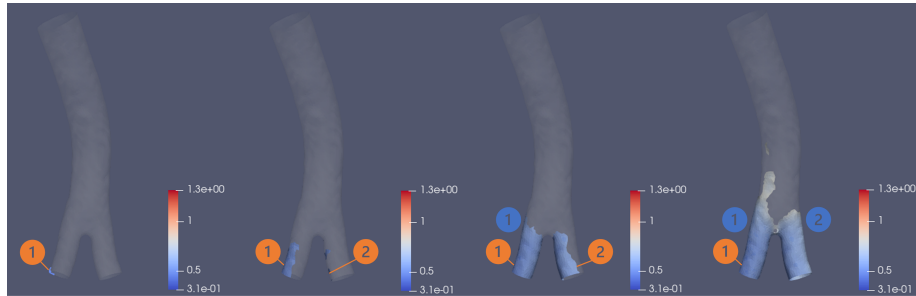
When the iliacs have comparable diameters there are two connected components born at similar values, resulting in two classes of 0-cycles that later merge together - as in Figure 6. The single class of 0-cycles with infinite persistence represents the closest point of the mesh to the centerline, the very first point appearing in the filtration. This class is always born at the iliacs, given their smaller radii. Moreover, the other iliac's first point induces the birth of a secondary early class of 0-cycles with high persistence. These components will be merged together as the radius value increases (see point “(1)” and “(2)” in Figure 6). For these reasons, each persistence diagram, except the ones with iliac aneurysm, have a high persistence point with birth coordinate given by the radius at which the second component is born and death coordinate given by the merging radius.

When an iliac aneurysm is present, it significantly deforms the lumen and so the minimal radius of the aneurysmatic iliac is greatly increased - see Figure 7. As a consequence the first point of the second iliac appears much later in the filtration, often after other points at the bifurcation region. Thus, instead of having two connected components born at similar times, we have a component that is expanding until it covers both iliacs. As a consequence, the absence of this second high persistence point in dimension 0 is a primary indicator for an iliac aneurysm.

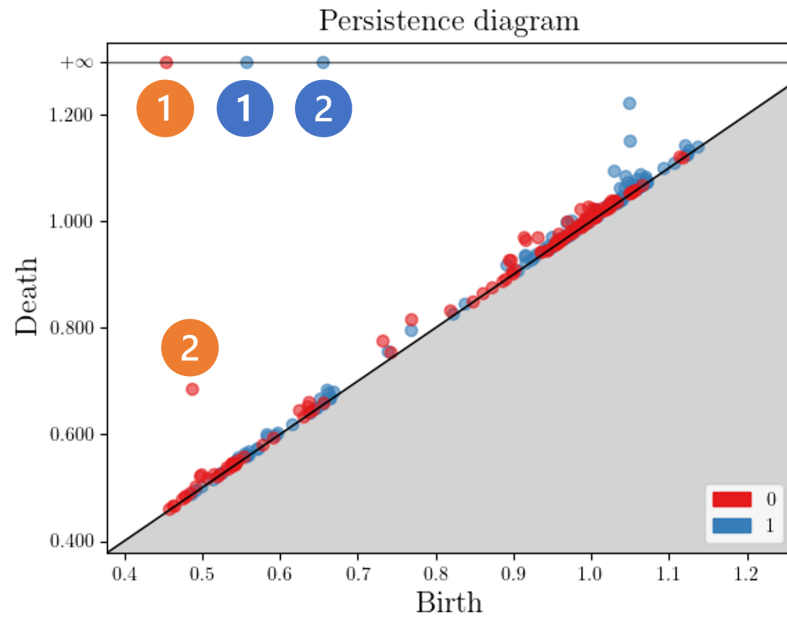
Similarly, any irregularity in the iliacs, inflating their lumen, may have the effect of delaying the birth of 1-cycles with infinite persistence. For instance, not having two classes of 1-cycles with infinite persistence born at roughly the same times (i.e. having roughly the same diameters) implies that one iliac is inflated. The only reasonable cause for that inflation is the presence of an aneurysm. Thus, if the two classes of 1-cycles with infinite persistence have a pronounced difference between their birth coordinates or have birth coordinates which are high (note that a 1-cycle is always going to appear at radius 1, around the neck), this indicates the presence of one or more aneurysms in that region of the blood vessels.

5.2.3 ABDOMINAL AORTIC ANEURYSM

We now focus on AAAs, which are obviously distinguished by large radial distances from the centerline and therefore by high values of birth and death coordinates of their associated points on the persistence diagram - see also Figure 8. But more can be said; in

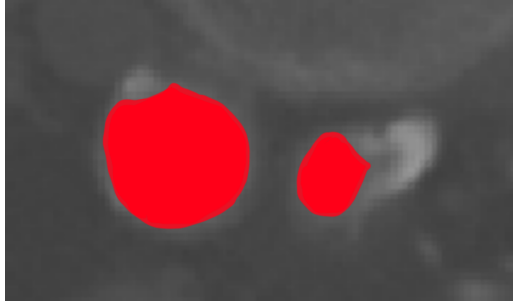


(a) Initial steps of the sublevel set filtration of a patient with healthy iliacs, showing the births of the iliacs-related persistence pairs: first appear the two local minima of the radial distance located on the two iliacs - orange (1) and (2) - and then the two loops going around the tubular structure of the iliacs - blue (1) and (2).

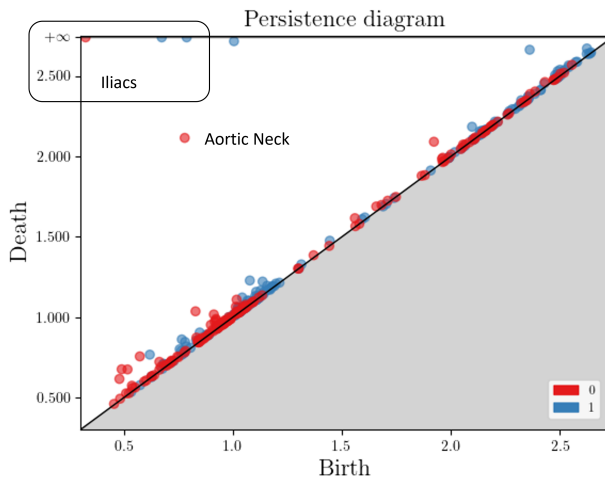


(b) The persistence diagram, in dimension 0 and 1, of an healthy patient, with highlighted the persistence pairs related to the iliacs, whose labels are coherent with the ones in Figure 6a.

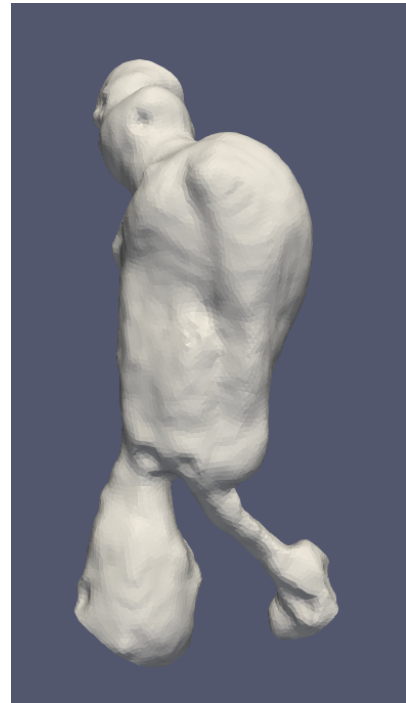
Figure 6: A visualization of the mesh of a healthy aorta with the birth and death of cycles related to the iliacs highlighted in the associated diagram.



(a) CTA scan slice of iliacs presenting calcification in the right iliac and aneurysm in the left. The red portion shows the lumen restriction created by calcifications and the bulge created by the aneurysm.



(b) The persistence diagram of a patient with an aortic aneurysm and an iliac aneurysm. The lack of an early 0-cycle with high persistence is visible. As is the presence of one class of high persistence 1-cycles created by the AAA.



(c) Mesh of the lumen of a patient being affected by calcifications and aneurysm in the iliacs: the left one presents a bulge created by the aneurysm, while the right one is severely occluded by calcifications.

Figure 7: CTA scan slice, mesh and persistence diagram of the same patient with a calcified (left) and aneurysmatic (right) iliac.

fact, persistence diagrams of patients affected by AAA are characterized by the following persistence pairs:

1. A notable and highly persistent class of 0-cycles is usually present when patients are affected by an AAA. These cycles are associated to the sudden increase of the distance from the centerline when moving from the aortic neck region to that part of the vessel where the AAA occurs. In fact, the presence of the AAA “splits” the aorta in two parts, separated by the AAA - see Figure 8. Along the filtration, each part generates a connected component; those two components merge only when it is possible to have a path across the aneurysm; see Figure 8.
2. Similarly, the AAA generates also a notable highly persistent class of 1-cycles, associated with the tubular structure of the neck, which doesn’t appear in healthy patients. As already mentioned AAA splits the blood vessel in two parts - see Figure 8. Each part has a loop going around the aorta. Only when all the aneurysm appears in the filtration the loop around the blood vessel on one side of the aneurysm and the one on the other, can be merged with each other and become equivalent. One of them therefore dies and the other one persists as structural persistence pair.

As a consequence, the corresponding point on the persistence diagram is easily recognizable since its birth is around the value 1.0 and its death has the highest value among all the points with finite persistence. Again, all of this is clearly visible in Figure 8.

To summarize, two main features make the persistence diagram of a patient with AAA easily distinguishable - see also Figure 8:

1. The presence of persistence pairs borning and dying at high distance values. In fact, no healthy aorta has a region with a distance from the centerline higher than 1.4, while the regions of an aneurysmal aorta can exceed the value of 7.0.
2. The presence of at least one 0-cycle and one 1-cycle classes with high persistence in the neck area (birth around 1).

5.2.4 CALCIFICATIONS

Calcifications are calcium deposits creating a local thickening of the aortic wall, on the internal side, resulting in indentations on the lumen’s surface, when in contact with the calcified wall. Thus, they produce local minima in the filtering function, as showcased in Figure 9. These inward bumps are picked up as 0-cycles with medium-persistence in the persistent diagram; see Figure 9b.

5.2.5 THROMBUS

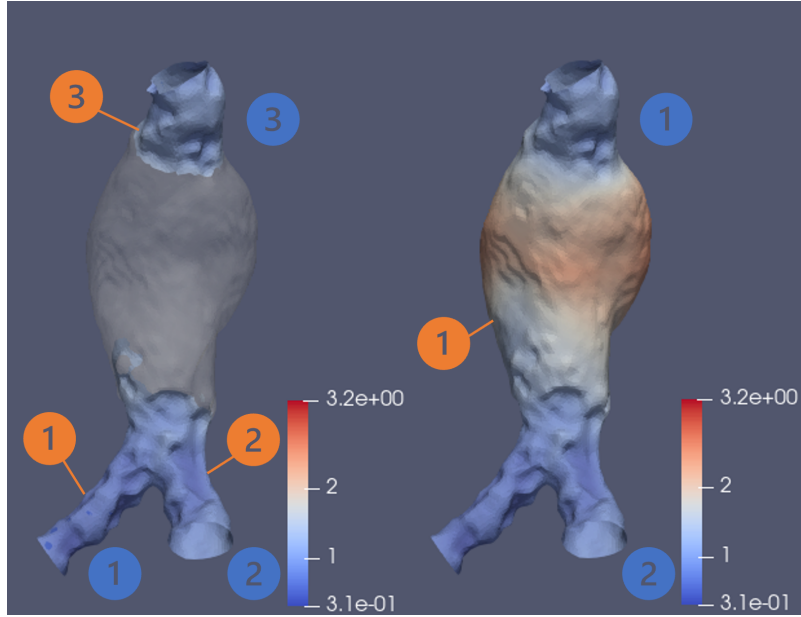
Lastly we consider blood vessels affected by a thrombus. A thrombus is often made by a non-homogeneous substance, which can flake off with the flow of blood creating wide ledges in the lumen (see Figure 10). It is most likely to be located in the area affected by AAA, due to the concentration of metabolites associated with inflammation. Thus, the presence of a pronounced thrombus produces a series of local maxima and/or minima, which induce 1 and 0 cycles in the persistence diagrams with relatively high birth coordinates and moderate persistence, see also Figure 12.

5.3 A detailed Example

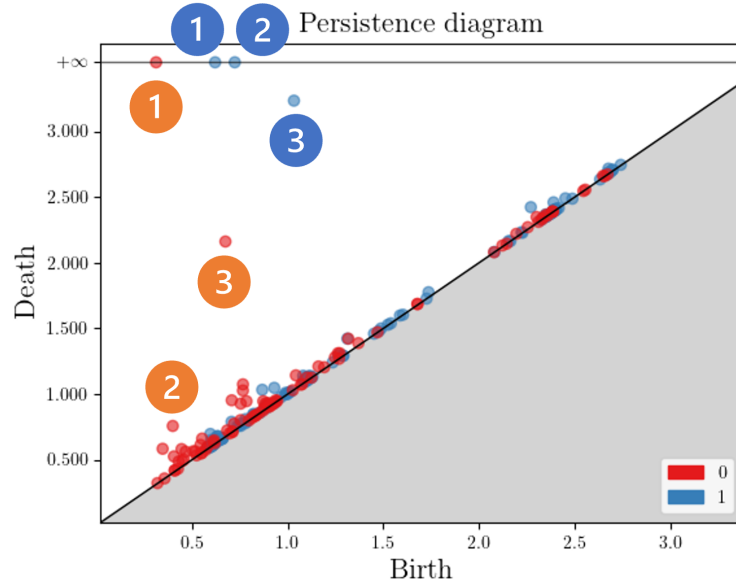
We now show an example of a concerning patient affected by AAA, iliac aneurysm and thrombus.

In Figure 11 we report the main steps of the sublevel set filtration of the selected patient. While in Figure 12 the associated persistence diagram is shown.

- At value 0.3 a 0-cycle of the first iliac appears.

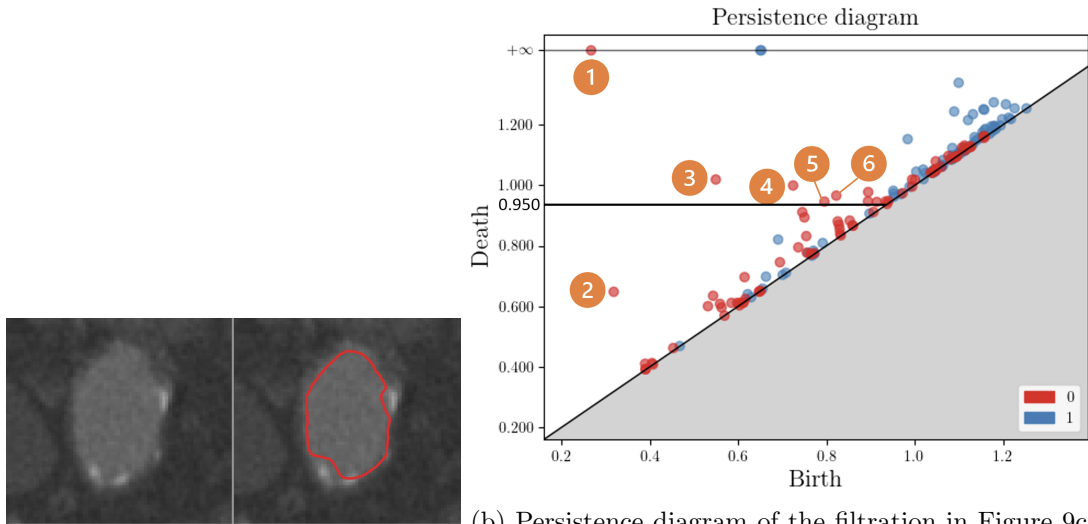


(a) Two different steps of the sublevel set filtration of a patient affected by AAA: in the first step we clearly see the two path connected components - orange (1), which is also merged with (2), and orange (3) - which are separated by the AAA. At very high filtration values the AAA is added to the filtration and the path connected components merge. A similar phenomenon involves also 1-cycles: on the left, the loop going around the upper portion of the aorta cannot “slide” down on the mesh and be equivalent to the loop going around the lower portion of the aorta - made by (1)+(2). This is instead possible on the right, causing the death of loop (3) at high values.



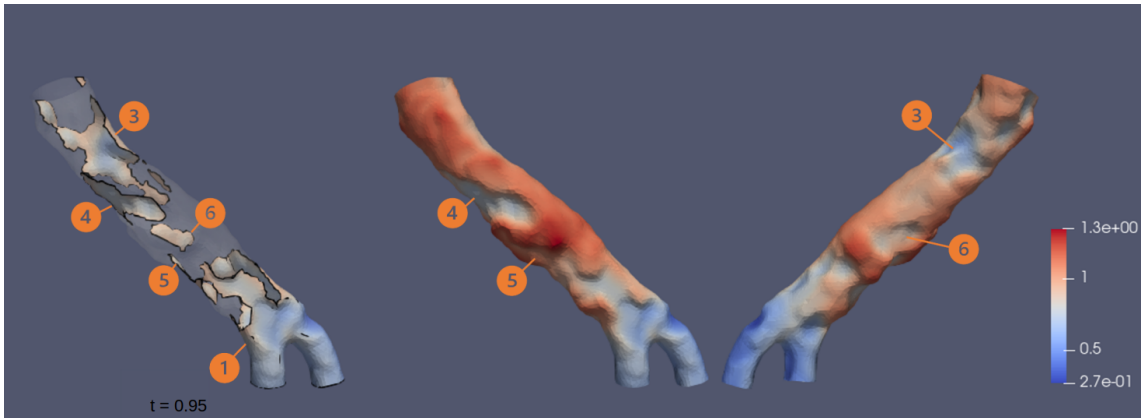
(b) Persistence diagram of the filtration in Figure 8a. We have highlighted the high persistence path connected component and loop caused by the AAA splitting in two parts the aorta.

Figure 8: The merging phenomena associated to AAA.



(a) CTA slice of a non-aneurysmal aorta with presence of calcifications which creates bump in the lumen of the blood i.e. with birth value higher than the aortic neck, as a consequence of the irregularities due to calcifications.

(b) Persistence diagram of the filtration in Figure 9c: we see a number of persistence pairs with medium persistence, being born in the main body of the aorta - i.e. with birth value higher than the aortic neck, as a consequence of the irregularities due to calcifications.



(c) Different time steps of the sublevel set filtration of an aorta without AAA but with calcifications: calcifications create many medium-sized irregularities and bumps in the lumen which are picked up by the filtration, creating a number of path connected components arising and persisting for some time.

Figure 9: Non-aneurysmal aorta with calcifications.

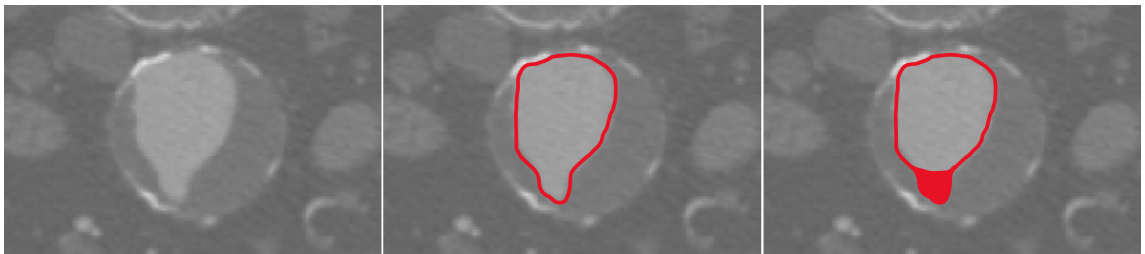


Figure 10: CTA slice of an AAA with thrombus occluding the lumen.

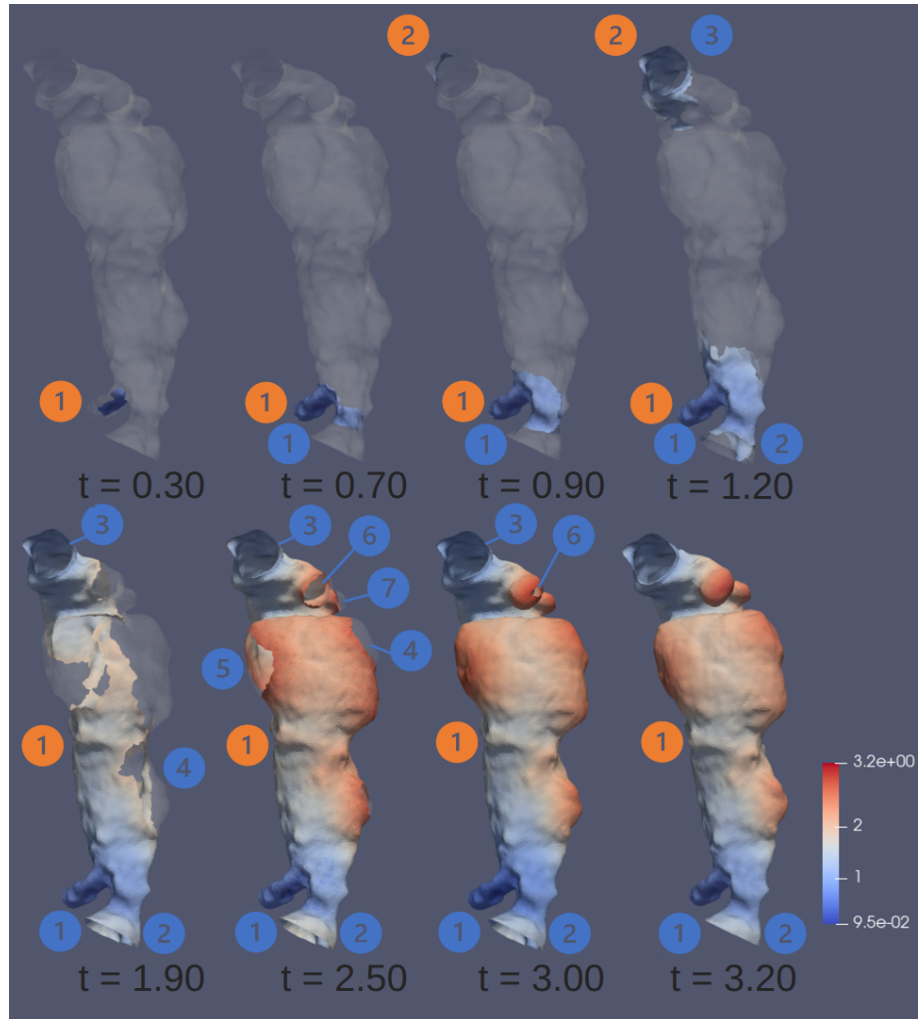


Figure 11: A patient affected by AAA, iliac aneurysm and thrombus. The filtration function values are reported in black on the bottom left corner of the aorta. The sublevel sets are represented by the highlighted portions of the mesh. The numbered features identify 0-dimensional (red) and 1-dimensional cycles associated to points in the diagram appearing in Figure 12.

- At value 0.7 a 1-cycle, around that iliac, appears. Note that the 0-cycles expands onto the other iliac without creating a new path connected component. There is in fact an aneurysm on the second iliac preventing the tapering of its extremity.
- At value 0.9 a novel 0-cycle appears on the aortic neck. The AAA separates this cycle from the one appeared in the beginning.
- At value 1.20 a 1-cycle going around the blood vessel appears.
- As the distance from the centerline increases - that is, the value of the radial filtration function increases -, the initial path connected component expands enclosing gradually also the AAA, connecting to and killing the path connected component and the loop associated to the neck. On the way, several classes of 1-cycles are created with high birth times; they are associated to the local maxima of the filtration function created in the aneurysmatic portion of the aorta by the thrombus.

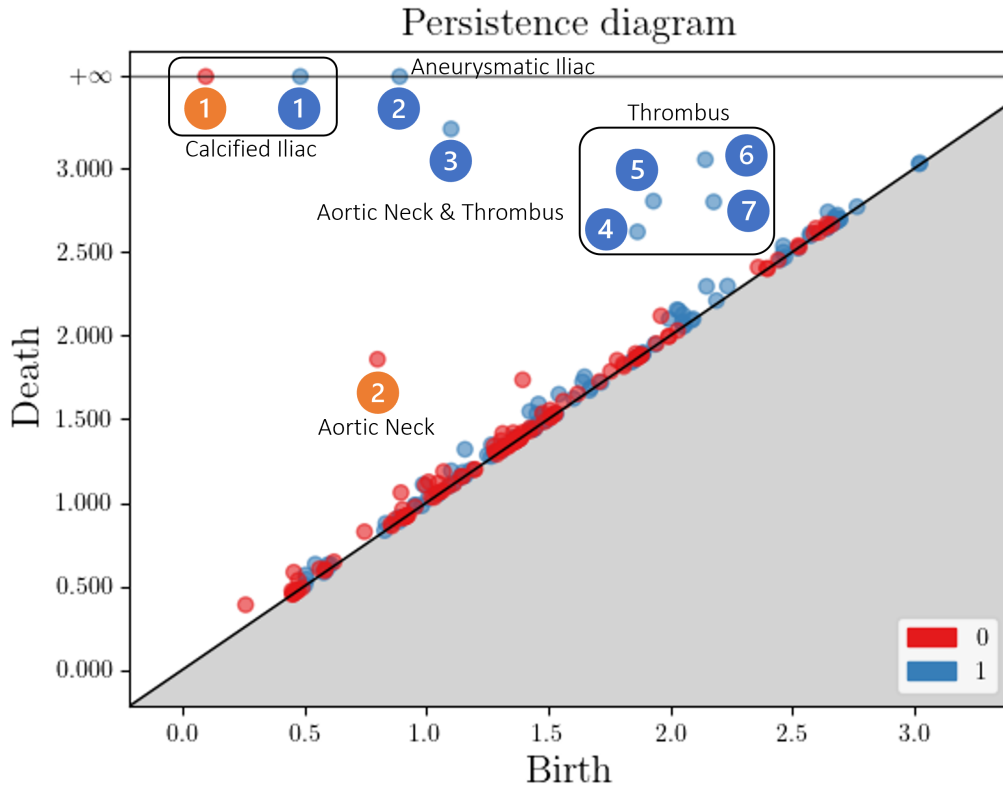


Figure 12: The persistence Diagram associated with the mesh shown in Figure 11. Features labelled as (1) both in dimension 0 and 1 are the structural pairs associated to the iliac which does not present an aneurysm. In particular, path connected component (1) is born very early along the filtration and that is because of some inwards bumps due to some calcifications. Persistence pairs (2) - both in dimension 0 and 1 -, instead, are born very late, almost at the filtration value of the neck. This is a clear consequence of the iliac aneurysm. The 1-cycles' class (3) is generated because of the AAA splitting the blood vessel in two parts. An in fact it dies at the latest value of the filtration. Then we have a group of 1-cycles - from (4) to (7) - with medium persistence, which reflect the irregularities in the lumen caused by some heterogeneous thrombus.

6. Population Analyses

The previous section discussed how persistent homology translates some relevant aortic features into persistence pairs shown as points of a persistence diagram. We now explore the behaviour of these topological summaries at the population level, to understand which kind of between patients variability can be captured with persistence diagrams.

We present two paradigmatic problems, both characterized by their simplicity: clustering and discrimination or, with different words, unsupervised and supervised classification of persistence diagrams. In the initial clustering exercise, we look for a natural stratification of persistence diagrams embedded in a metric space endowed with a Wasserstein metric. Secondly, we exploit the analysis of Section 5 to introduce a supervised classification pipeline aimed at the construction of classifiers identifying patients with: (1) AAA, (2) calcifications, (3) thrombus, (4) iliac aneurysm.

6.1 Clustering

Throughout the manuscript we argued that irregularities in the aortas are represented by inward and outward bumps, representing pathologies of different nature, which are captured separately by 0-cycles or 1-cycles represented as persistence pairs in a persistence diagram.

Since both the persistent diagrams for classes of 0-cycles and 1-cycles are relevant to capture shape differences between aortas, we introduce the following family of metrics between patients P_i and P_j :

$$d_p^p(P_i, P_j) = \lambda \cdot W_p^p(D_i^0, D_j^0) + (1 - \lambda) \cdot W_p^p(D_i^1, D_j^1),$$

where $p \geq 1$, $\lambda \in [0, 1]$ and, for $k = 0, 1$, the persistence diagrams D_i^k, D_j^k are those for the k -cycles of patient i and j respectively; W_p is the p -Wasserstein distance introduced in (1). Note that, by setting $p = \infty$, one obtains the weighted average of the bottleneck distances between the diagrams. Although different mixing weights are allowed, in the following we set $\lambda = 0.5$ for simplicity. Tailoring the choice of λ could benefit the analysis of specific classification problems.

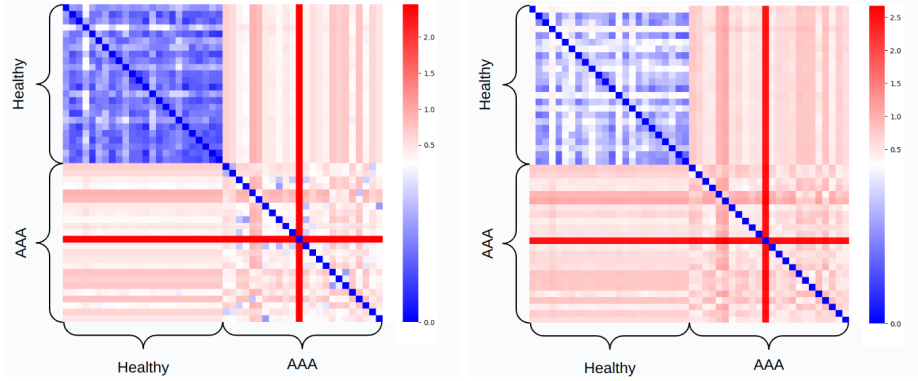
Figure 13 depicts the matrices of pairwise distances between patients in the cohort of our study, when $p = \infty$ and $p = 2$ respectively. Statistical units have been ordered so that healthy patients come before those with an AAA: indeed, $H01, \dots, H24$ index the healthy patients without AAA while $A01, \dots, A24$ indicate the patients with AAA. By visual inspection, it is clear, both in Figure 13b and Figure 13a, that this grouping is very well captured by both distance matrices. In fact, visualizing a low-dimensional representations, obtained by MultiDimensional Scaling (MDS), of the metric spaces embedding the persistence diagrams – see Figure 13d and Figure 13c – we immediately notice how patients without AAA are clustered together, while the presence of an AAA, by introducing high persistence points in the persistence diagram, generates a larger variability in the MDS representation of the persistence diagrams of diseased patients - see Section 5.2.3.

This grouping can indeed be captured by a clustering algorithm. For instance we report the dendrograms relative to agglomerative hierarchical clustering run with Ward linkage, in Figure 14b and Figure 14a. Leaves are coloured as in Figure 13d and Figure 13c.

6.2 Supervised classification - AAA

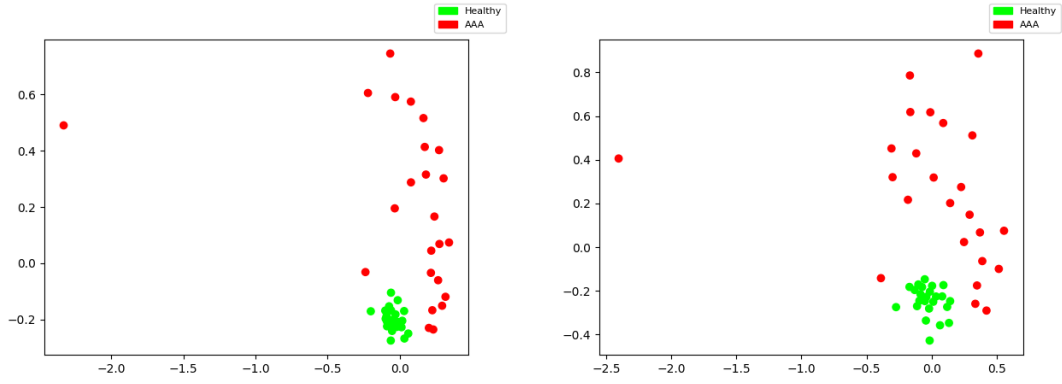
In Section 6.1 we reported an unsupervised algorithmic pipeline which generates a very clear clusterization of the topological representations of the patients in our study. We now setup a supervised classification algorithm aimed at discriminating patients with an AAA from the others.

The dendrograms in Figure 14 justify the use of a very simple algorithm like k -nearest neighbors (KNN). We report the leave-one-out (l1out) confusion matrices in Figure 15 for $k = 5$. We point out that for any choice of $k \in \{1, \dots, 5\}$ we get 97% accuracy, with the only missclassified patient being always the same one, visibly close to the healthy patients



(a) Matrix of pairwise p -Wasserstein distances between persistence diagrams, with $(p = \infty)$. Patients are ordered so that healthy patients come before non-healthy ones.

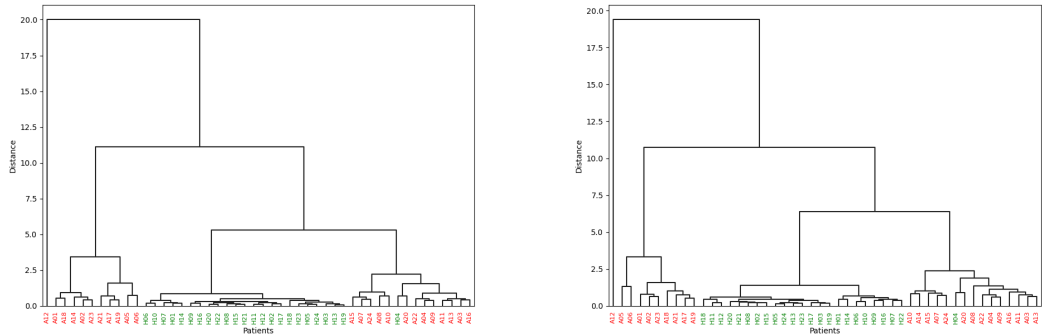
(b) Matrix of pairwise p -Wasserstein distances between persistence diagrams, with $(p = 2)$. Patients are ordered so that healthy patients come before the ones affected by AAA.



(c) Two dimensional MDS representation of the matrix in Figure 13a.

(d) Two dimensional MDS representation of the matrix in Figure 13b.

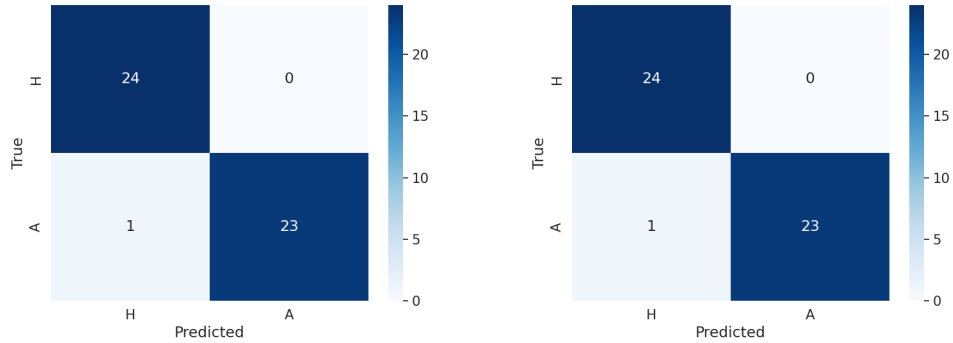
Figure 13: Pairwise distance matrices and low-dimensional embeddings for the cohort of patients described in Section 6.1.



(a) Hierarchical clustering dendrogram with the previously defined Bottleneck distance and Ward linkage.

(b) Hierarchical clustering dendrogram with the previously defined 2-Wasserstein distance and Ward linkage.

Figure 14: Hierarchical clustering dendrograms related to the clustering problem presented in Section 6.1. Patients in red are affected by AAA, while healthy ones are drawn in green.



(a) Leave-one-out confusion matrix for the classification case study presented in Section 6.2, starting from the matrix obtained with the bottleneck distance. (b) Leave-one-out confusion matrix for the classification case study presented in Section 6.2, starting from the matrix obtained with the 2-Wasserstein.

Figure 15: Confusion matrices for the classification case study presented in Section 6.2. Label A is for patients with AAA, H for the "healthy" ones.

also in Figure 13. This patient has been checked by the collaborating clinicians and it has been regarded as having a relatively small AAA.

6.3 Supervised classification - Calcifications

We now want to discriminate patients with calcifications from the others. To do so, we rely on Section 6.3: therein we showed that calcifications appear as mid-persistence features in the zero dimensional persistence diagram, being local minima of the radial filtering function.

Thus, for all patients, we count the number of 0 dimensional persistence pairs with persistence greater than or equal to a threshold and less than ∞ . Patients with or without calcifications have been identified and labelled by looking at their TAC, with the help of a collaborating clinician; the threshold τ_p for persistence has been set to 0.1, a value coherent with Section 5.1. Results are shown in Figure 16: all patients whose count of filtered persistence pairs exceeds the threshold τ_c of 3 are classified as affected by calcification. Both thresholds τ_p and τ_c have been selected to maximize leave-one-out accuracy; the values $\tau_p = 0.1$ and $\tau_c = 3$ result in only one leave-one-out misclassified patient. Maximization has been obtained through grid search; for τ_p the grid spans a range from 0.005 to 0.5, with increments of 0.005, while for τ_c it considers the natural numbers from 1 up to 20.

Note that, as shown by Figure 16, identifying patients with calcifications is more of a problem for those without an AAA - the S patients in the left half of Figure 16 - since almost all patients with an AAA show also the presence of calcifications.

6.4 Supervised classification - Iliac Aneurysm

We now deal with iliac aneurysms. As discussed in Section 5.2.2, we expect an aneurysm in the iliac area to show up in the persistence diagram in two different ways: 1) the absence of a class of 0-cycles born on the affected iliac, separately from the one encompassing the healthy one; 2) one or two classes of 1-cycles with infinite persistence, born at high times. Since the absence of the second class of 0-cycles is redundant with respect to the information of the birth of the second class of 1-cycles, we just consider as features for this classification problem the birth coordinates of the two classes of 1-cycles with infinite persistence, ordered according to their birth. We call those two variables B_1 and B_2 . The difference between patients with or without an iliac aneurysm, it's evident in Figure 17a:

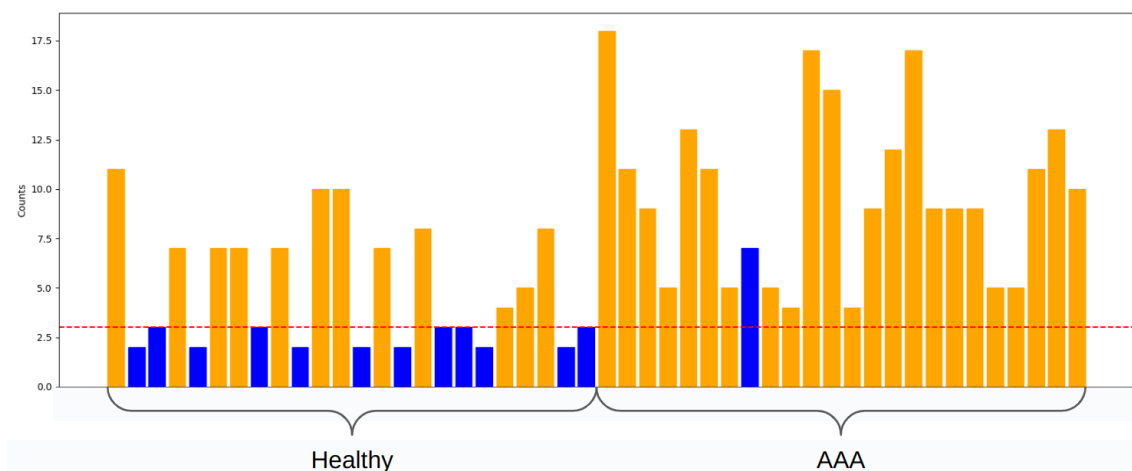
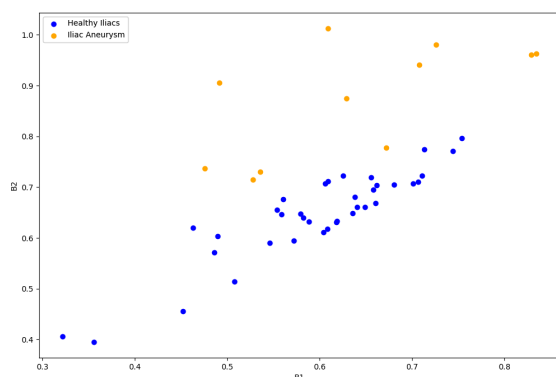
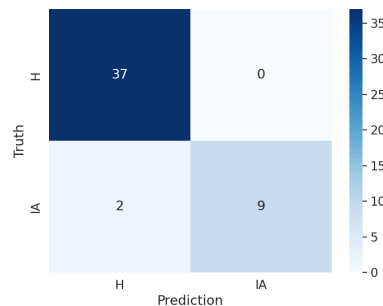


Figure 16: Plot related to Section 6.3, representing the counts of the persistence pairs in dimension 0 with persistence greater than 0.1 to recognize patients with calcifications. Patients which present calcifications are plotted in orange, the others in blue. There is clearly correlation between the presence of calcifications and irregularities of the lumen captured by 0 dimensional homology. And we highlight that this holds true also for healthy patients, which is arguably the more interesting situation, as most of the patients affected by AAA present also calcifications. Patients are labelled and ordered as in previous figures.



(a) Scatterplot of the variables B_1 and B_2 used for classifying patients with iliac aneurysm.



(b) L1out confusion matrix for Iliac Aneurysm classification. Label AI is for patients with iliac aneurysm, H for the others.

Figure 17: Iliac Aneurysm classification, Section 6.4.

large values of birth for both 1-cycles are associated to the presence of an iliac aneurysm. In particular the second coordinate, i.e. the largest birth, is the most discriminating factor. This is coherent with the fact that having one iliac aneurysm increases the birth coordinate of the second class of 1-cycles with infinite persistence; while two aneurysms increase both coordinates. Thus the second feature is always altered by the presence of an aneurysm at the iliacs.

We fit a linear discriminant analysis model; by leave-one-out, this predicts correctly all patients but two. The confusion matrix is reported in Figure 17b. Both misclassified patients are affected by iliac aneurysms, but classified as healthy by our pipeline: their aneurysms are indeed not severe, according to the collaborating clinicians.

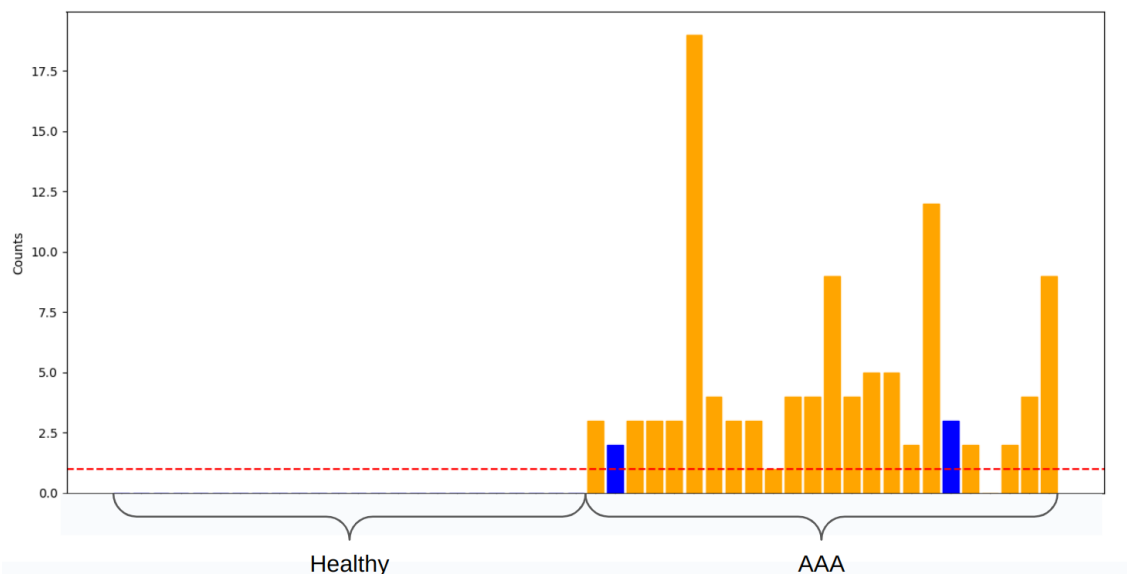


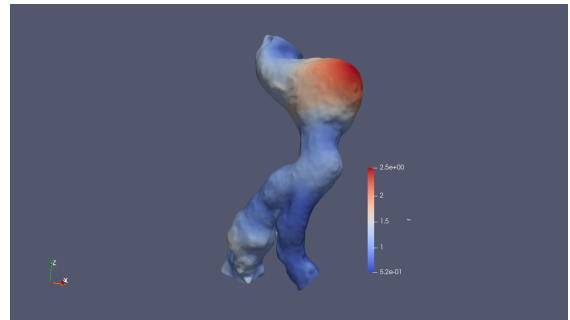
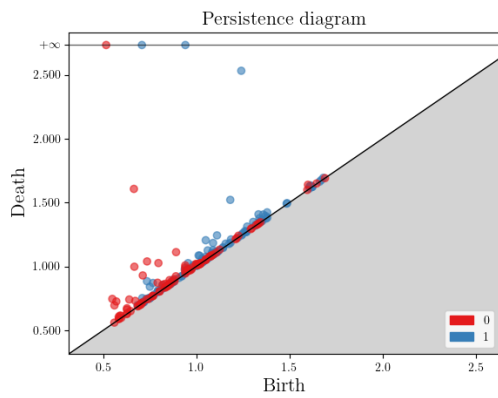
Figure 18: Plot related to Section 6.5, representing the counts of persistence pairs with medium persistence associated to irregularities of the lumen, trying to exclude bumps located on the iliacs and on the aortic neck. Patients which present thrombi are plotted in orange, the others in blue. Again we can see correlation between the presence of thrombi and irregularities of the lumen captured by the selected points in 0 dimensional homology.

6.5 Supervised classification - Thrombus

Lastly, we turn to the problem of detecting thrombi, which have been discussed in Section 5.2.5. We have argued that thrombi are characterized by irregularities in the lumen, most likely in the part of the blood vessel which is affected by AAA. Depending on the homogeneity of the obstruction, these irregularities might generate local maxima of the radial filtering function.

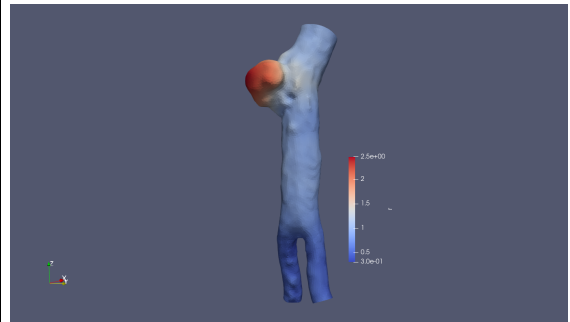
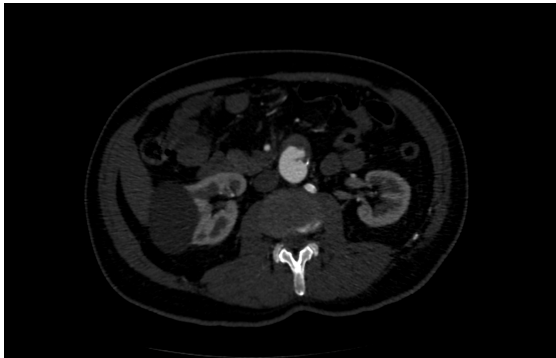
We approach thrombus classification by filtering out points in the persistence diagram and retaining only 0 and 1 dimensional persistence pairs with finite persistence and high birth coordinates.

In particular, for each diagram, we retain 0-cycles and 1-cycles with birth coordinate larger than or equal to 1.1 - so that we know we are not on the iliacs and the neck - and persistence larger then or equal to 0.1 - to filter out smaller and noisy bumps. Disregarding the label declaring if they are 0-cycles or 1-cycles, the number of cycles retained for each patient is shown in Figure 18; note that all healthy patients do not present any thrombi. Thus, we can label as affected by thrombus all patients with at least 2 retained classes of cycles, obtaining four missclassified patients: A10, A19, A20, A21. In Figure 19 we report data about two of these patients, to understand the roots of this classification errors. For instance, patient A20 is without thrombi but is classified as a having one. We can see in Figure 19a some high persistence features in dimension 1, which are induced by a very irregular lumen, with multiple aneurysm-like dilations. But no thrombus. Instead patient A10 is affected by thrombi but classified as not having any. The reason can be clearly seen in Figure 19d: the thrombus outside the lumen is very homogeneous, resulting in a very straight and regular lumen, with no bumps. By construction, our methodology is good at capturing information contained in inwards and outwards bumps, so the persistence diagrams of patient A10 are similar to those of a healthy patient. However, we do believe that segmenting also the thrombi from the CTA scans could solve this issue. We leave this further investigation to future works.



(a) Patient A20 missclassified by the analysis in Section 6.5.

(b) The patient A20 missclassified by the analysis in Section 6.5.



(c) Patient A10 missclassified by the analysis in Section 6.5.

(d) Patient A10 missclassified by the analysis in Section 6.5.

Figure 19: Patients missclassified by the analysis in Section 6.5.

7. Software and Packages

The segmentation pipeline makes use of *vmtk 1.4.0* Antiga et al. (2008), a collection of libraries and tools for 3D reconstruction and surface data analysis of blood vessels Antiga (2002).

The software used to visualize all the meshes and CTA scans shown in these pages is *Paraview* Ahrens et al. (2005) version *5.11.0*.

Persistence diagrams and related distances are computed using the python library *gudhi* Maria et al. (2014) version 3.8.0, while for clusterization and visualization purposes the libraries *scikit-learn* Pedregosa et al. (2011), *scipy* Virtanen et al. (2020), *seaborn* Waskom (2021) and *matplotlib* Hunter (2007) have been adopted.

8. Discussion and conclusion

We presented a complex pipeline to work with data obtained from medical imaging of abdominal aortas, exploiting the tools of topological data analysis. Each reconstructed mesh of an abdominal aorta is represented by an object called persistence diagram, displaying the 0-cycles and the 1-cycles characterizing a radial filtration function defined on the mesh. These diagrams are able to concisely summarize many shape-related features of the blood vessel, related to the irregularities of its lumen, which appear as a consequence of abdominal aortic aneurysms and some related features, like calcifications and intra-luminal thrombi.

We argue that the proposed representation could lead to advances in the data analysis of AAAs. To support our claim we exhibit the results of several classification exercises, built upon a training set of persistent diagrams derived by 48 CTA scans, 24 of which picture a aneurysmal aorta.

The take home message is that relying on a persistence diagram representation makes most of these classification exercises almost straightforward, due to the amount of information collected by these easy-to-handle mathematical objects. Moreover, because of the unsettling difference with more classical feature-gathering methods, we devoted a consistent part of this work to stress the interpretability of the rich information displayed by persistence diagrams.

Natural further developments of this work will tackle the forecasting and regression problems which have already captured the attention of the medical and statistical communities, like estimating growth rates of AAA, indication to surgery and rupture's risks. To that end, persistence diagrams present a number of mathematical advantages, briefly mentioned in the manuscript, allowing for more refined object oriented data analysis which will be the focus of our future works.

9. Acknowledgements

Piercesare Secchi acknowledges the support by MUR, grant Dipartimento di Eccellenza 2023-2027.

Maurizio Domanin acknowledges the support of Irene Fulgheri for the help with Fondazione IRCCS Cà Granda Ospedale Maggiore Policlinico's ethical committee.

Appendix A. Average Neck Radius

Neck’s average radius has been estimated with the following steps:

1. Linear interpolation of the centerline’s points.
2. For a given parameter $s = 0.5mm$, empirically chosen, starting at the neck seed’s height s_0 on the centerline, find the points s_i at distance s on the curvilinear abscissa.
3. For each of the s_i points find the planes P_i . orthogonal to the centerline in s_i . For each of the planes P_i identified, a *fitting ellipse* of the mesh points is built, following the Fitzgibbon’s approach Fitzgibbon et al. (1999); Halir and Flusser (2000), and its semi-major and semi-minor axes M_i and m_i are computed. In some cases the slice can identify more regions; when this verifies, the ellipse is built using only the region of points that contains the point s_i .
4. Starting from the initial seed s_0 , a check is made for all the planes P_j found. If the two proposition:

$$\frac{|M_i - M_{i+j}|}{M_i} < 0.10 \quad \forall j = 1, \dots, k \quad \text{with } k=10 \text{ (5 mm)} \quad (2a)$$

$$M_i < 22.5mm \quad (2b)$$

hold, M_i and m_i are collected. The first and all the following s_i that do not respect the proposition are discarded. k is chosen empirically and the conditions are made in order to control both the raw AAA’s diameter and its relative growth.

5. The result is the mean of the mean of M_i and m_i for each s_i that is not discarded. In this way we obtain an accurate approximation of the neck’s radius.

References

- H. Adams, Tegan Emerson, M. Kirby, R. Neville, C. Peterson, P. Shipman, Sofya Chepushtanova, E. Hanson, F. Motta, and Lori Ziegelmeier. Persistence images: A stable vector representation of persistent homology. *Journal of Machine Learning Research*, 18(1):1–35, 2017.
- James Ahrens, Berk Geveci, Charles Law, C Hansen, and C Johnson. 36-paraview: An end-user tool for large-data visualization. *The visualization handbook*, 717:50038–1, 2005.
- Luca Antiga. *Patient-Specific Modeling of Geometry and Blood Flow in Large Arteries*. PhD thesis, Politecnico di Milano, 2002.
- Luca Antiga, Marina Piccinelli, Lorenzo Botti, Bogdan Ene-Iordache, Andrea Remuzzi, and David A Steinman. An image-based modeling framework for patient-specific computational hemodynamics. *Medical & biological engineering & computing*, 46:1097–1112, 2008.
- Christophe AN Biscio and Jesper Møller. The accumulated persistence function, a new useful functional summary statistic for topological data analysis, with a view to brain artery trees and spatial point process applications. *Journal of Computational and Graphical Statistics*, 28(3): 671–681, 2019.
- Peter Bubenik. Statistical topological data analysis using persistence landscapes. *Journal of Machine Learning Research*, 16(3):77–102, 2015.
- F. Chazal, Brittany Terese Fasy, F. Lecci, A. Rinaldo, and L. Wasserman. Stochastic convergence of persistence landscapes and silhouettes. *Journal of Computational Geometry*, 6(2):140–161, 2015.
- David Cohen-Steiner, Herbert Edelsbrunner, and John Harer. Stability of persistence diagrams. In *Proceedings of the twenty-first annual symposium on Computational geometry*, pages 263–271, 2005.

- M. M. Dua and R. L. Dalman. Hemodynamic influences on abdominal aortic aneurysm disease: Application of biomechanics to aneurysm pathophysiology. *Vascular Pharmacology*, 53(1):11–21, 3 2010.
- Herbert Edelsbrunner and John L Harer. *Computational topology: an introduction*. American Mathematical Society, 2022.
- Andrew Fitzgibbon, Maurizio Pilu, and Robert B. Fisher. Direct least square fitting of ellipses. *IEEE Transactions on Pattern Analysis and Machine Intelligence*, 21(5):476–480, 5 1999.
- Robert Fosbinder and Denise Orth. *Essentials of Radiologic Science*. Lippincott Williams & Wilkins, 2011.
- Radim Halir and Jan Flusser. Numerically stable direct least squares fitting of ellipses. *IEEE Transactions on Pattern Analysis and Machine Intelligence*, 21, 5 2000.
- K. Hirata, T. Nakaura, M. Nakagawa, and et al. Machine learning to predict the rapid growth of small abdominal aortic aneurysm. *Journal of Computed Assisted Tomography*, 44(1):37–42, 01 2020.
- John D Hunter. Matplotlib: A 2d graphics environment. *Computing in science & engineering*, 9 (03):90–95, 2007.
- Claude Kauffmann, An Tang, Éric Therasse, Marie-France Giroux, Stephane Elkouri, Philippe Melanson, Bertrand Melanson, Vincent L Oliva, and Gilles Soulez. Measurements and detection of abdominal aortic aneurysm growth: accuracy and reproducibility of a segmentation software. *European journal of radiology*, 81(8):1688–1694, 2012.
- Hyangkyoung Kim, Tae-Won Kwon, Eol Choi, Seonjeong Jeong, Hong-Kyu Kim, Youngjin Han, Yong-Pil Cho, Hyun-Ki Yoon, Jaewon Choe, and Won Hong Kim. Aortoiliac diameter and length in a healthy cohort. *PLOS ONE*, 17(5):1–13, 5 2022. doi: 10.1371/journal.pone.0268077. URL <https://doi.org/10.1371/journal.pone.0268077>.
- N. Kontopodis, M. Klontzas, K. Tzirakis, S Charalambous, K. Marias, D. Tsetis, A. Karantanas, and C. V. Ioannou. Prediction of abdominal aortic aneurysm growth by artificial intelligence taking into account clinical, biologic, morphologic, and biomechanical variables. *Vascular*, 31 (3):409–416, 06 2023.
- F. Kyriakou, W. Dempster, and D. Nash. A methodology to quantify the geometrical complexity of the abdominal aortic aneurysm. *Scientific Reports*, 9, 11 2019a.
- Faidon Kyriakou, William Dempster, and David Nash. A methodology to quantify the geometrical complexity of the abdominal aortic aneurysm. *Scientific Reports*, 9(1):17379, 2019b.
- R. Lee, D. Jarchi, R. Perera, and et al. Applied machine learning for the prediction of growth of abdominal aortic aneurysm in humans. *EJVES Short Reports*, 39:24–28, 05 2018.
- Moritz Lindquist Liljeqvist, Marko Bogdanovic, Antti Siika, T Christian Gasser, Rebecka Hultgren, and Joy Roy. Geometric and biomechanical modeling aided by machine learning improves the prediction of growth and rupture of small abdominal aortic aneurysms. *Scientific Reports*, 11 (1):18040, 2021.
- Clément Maria, Jean-Daniel Boissonnat, Marc Glisse, and Mariette Yvinec. The gudhi library: Simplicial complexes and persistent homology. In *Mathematical Software–ICMS 2014: 4th International Congress, Seoul, South Korea, August 5-9, 2014. Proceedings 4*, pages 167–174. Springer, 2014.
- James Stephen Marron and Ian L Dryden. *Object oriented data analysis*. CRC Press, 2021.
- K. Mealy and A. Salman. The true incidence of ruptured abdominal aortic aneurysms. *Medical engineering & physics*, 2(2):405–408, 12 1988.

- James R Munkres. *Elements of algebraic topology*. CRC press, 2018.
- Adam Parr, Chanaka Jayaratne, Petra Buttner, and Jonathan Golledge. Comparison of volume and diameter measurement in assessing small abdominal aortic aneurysm expansion examined using computed tomographic angiography. *European journal of radiology*, 79(1):42–47, 2011.
- Ole Martin Pedersen, Aslak Aslaksen, and Vik-Mo Harald. Numerically stable direct least squares fitting of ellipses. *Journal of Vascular Surgery*, 17, 3 1993.
- Fabian Pedregosa, Gaël Varoquaux, Alexandre Gramfort, Vincent Michel, Bertrand Thirion, Olivier Grisel, Mathieu Blondel, Peter Prettenhofer, Ron Weiss, Vincent Dubourg, et al. Scikit-learn: Machine learning in python. *the Journal of machine Learning research*, 12:2825–2830, 2011.
- M. Piccinelli, C. Vergara, L. Antiga, L. Forzenigo, P. Biondetti, and M. Domanin. Impact of hemodynamics on lumen boundary displacements in abdominal aortic aneurysms by means of dynamic computed tomography and computational fluid dynamics. *Biomechanics and Modeling in Mechanobiology*, 12(6):1263–1276, 11 2013.
- B. Sonesson, T. Länne, F. Hansen, and T. Sandgren. Infrarenal aortic diameter in the healthy person. *European Journal of Vascular and Endovascular Surgery*, 8(1):89–95, 1 1994.
- Milan Sonka and J. Michael Fitzpatrick. *Handbook of Medical Imaging, Volume 2. Medical Image Processing and Analysis*. SPIE, 2009.
- C. Vergara, D. Le Van, M. Quadrio, and et al. Large eddy simulations of blood dynamics in abdominal aortic aneurysms. *Medical Engineering and Physics*, 47:38–46, 2017.
- Pauli Virtanen, Ralf Gommers, Travis E Oliphant, Matt Haberland, Tyler Reddy, David Cournapeau, Evgeni Burovski, Pearu Peterson, Warren Weckesser, Jonathan Bright, et al. Scipy 1.0: fundamental algorithms for scientific computing in python. *Nature methods*, 17(3):261–272, 2020.
- Michael L Waskom. Seaborn: statistical data visualization. *Journal of Open Source Software*, 6(60):3021, 2021.
- K. A. Wilson, J. S. Lindholt, P. R. Hoskins, and et al. The relationship between abdominal aortic aneurysm distensibility and serum markers of elastin and collagen metabolism. *European Journal of Vascular and Endovascular Surgery*, 21(2):175–178, 2 2001.
- Chengcheng Zhu, Joseph R Leach, Yuting Wang, Warren Gasper, David Saloner, and Michael D Hope. Intraluminal thrombus predicts rapid growth of abdominal aortic aneurysms. *Radiology*, 294(3):707–713, 2020.